The Monitor project: JW 380 – a 0.26-, 0.15-M⊙, pre-main-sequence eclipsing binary in the Orion nebula cluster

Jonathan Irwin,[1]* Suzanne Aigrain,[1,2] Simon Hodgkin,[1] Keivan G. Stassun,[3]
Leslie Hebb,[4] Mike Irwin,[1] Estelle Moraux,[5] Jerome Bouvier,[5] Aude Alapini,[2]
Richard Alexander,[6] D. M. Bramich,[7] Jon Holtzman,[8] Eduardo L. Martín,[9]
Mark J. McCaughrean,[2] Frédéric Pont,[10] P. E. Verrier[1]
and María Rosa Zapatero Osorio[9]

[1]*Institute of Astronomy, University of Cambridge, Madingley Road, Cambridge CB3 0HA*
[2]*Astrophysics Group, School of Physics, University of Exeter, Stocker Road, Exeter EX4 4QL*
[3]*Department of Physics and Astronomy, Vanderbilt University, VU Station B 1807, Nashville, TN 37235, USA*
[4]*School of Physics and Astronomy, University of St Andrews, North Haugh, St Andrews KY16 9SS*
[5]*Laboratoire d'Astrophysique, Observatoire de Grenoble, BP 53, F-38041 Grenoble Cédex 9, France*
[6]*JILA, University of Colorado, Boulder, CO 80309-0440, USA*
[7]*Isaac Newton Group of Telescopes, Apartado de Correos 321, E-38700 Santa Cruz de la Palma, Canary Islands, Spain*
[8]*Astronomy Department, New Mexico State University, Las Cruces, NM 88003, USA*
[9]*Instituto de Astrofísica de Canarias, C/Vía Láctea, s/n E38205, La Laguna, Tenerife, Spain*
[10]*Observatoire Astronomique de l'Université de Genève, 51 chemin des Maillettes, CH-1290 Sauverny, Switzerland*

ABSTRACT

We report the discovery of a low-mass (0.26 ± 0.02, 0.15 ± 0.01 M⊙) pre-main-sequence (PMS) eclipsing binary (EB) with a 5.3 d orbital period. JW 380 was detected as part of a high-cadence time-resolved photometric survey (the Monitor project) using the 2.5-m Isaac Newton Telescope and Wide Field Camera for a survey of a single field in the Orion nebula cluster (ONC) region in V and i bands. The star is assigned a 99 per cent membership probability from proper motion measurements, and radial velocity observations indicate a systemic velocity within 1σ of that of the ONC. Modelling of the combined light and radial velocity curves of the system gave stellar radii of $1.19^{+0.04}_{-0.18}$ and $0.90^{+0.17}_{-0.03}$ R⊙ for the primary and the secondary, with a significant third light contribution which is also visible as a third peak in the cross-correlation functions used to derive radial velocities. The masses and radii appear to be consistent with stellar models for 2–3 Myr age from several authors, within the present observational errors. These observations probe an important region of mass–radius parameter space, where there are currently only a handful of known PMS EB systems with precise measurements available in the literature.

Key words: surveys – binaries: eclipsing – stars: individual: JW 380 – stars: pre-main-sequence – open clusters and associations: individual: Orion nebula cluster.

1 INTRODUCTION

Detached eclipsing binaries (EBs) provide one of the most precise ($\lesssim 2$ per cent) and accurate (largely model- and distance-independent) methods for measurement of fundamental stellar properties (particularly, masses and radii). These can be used to place stringent constraints on stellar evolution models.

On the pre-main-sequence (PMS), such constraints are presently extremely scarce below 1 M⊙, and to our knowledge there are only

five known PMS EB systems in this mass range. These are a 1.0, 0.7 M⊙ EB (Stassun et al. 2004) and a 1.27, 0.93 M⊙ EB (Covino et al. 2001, 2004), both in Orion (the former is thought to belong to the Ori 1c association), with corresponding age ∼5–10 Myr, an M-dwarf EB in NGC 1647 (∼150 Myr; Hebb et al. 2006), and two EBs in the Orion nebula cluster (ONC): a brown dwarf–brown dwarf system (Stassun, Mathieu & Valenti 2006, 2007) and a 0.4, 0.4 M⊙ M-dwarf EB (Cargile, Stassun & Mathieu, submitted). Comparison of the NGC 1647 and ONC brown dwarf systems to a variety of stellar models (specifically Baraffe et al. 1998; Siess, Forestini & Dougados 1997; Girardi et al. 2000; Yi et al. 2001 for the former, and Burrows et al. 1997; D'Antona & Mazzitelli 1997; Baraffe et al.
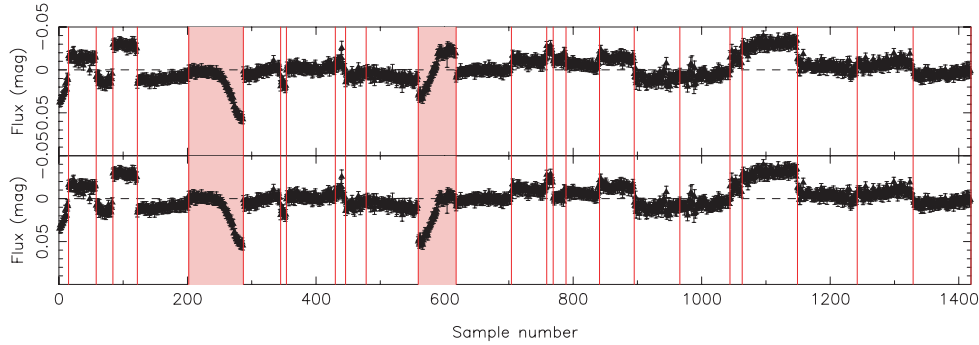
*E-mail: jmi@ast.cam.ac.uk

Figure 1. INT/WFC *i*-band light curve, plotted as a function of sample number (numbering from 1 for the first observation). Vertical lines denote the boundaries between different nights. The horizontal dashed line indicates the median light-curve level. The upper panel shows the data, and the lower panel the data with the median light-curve level subtracted from nights containing eclipses (the nights which were modified are shaded in the figure), to reduce the effect of the out-of-eclipse variations on the measured eclipse depths.

1998 for the latter) by the respective authors has indicated that none fits both components of the binaries simultaneously. In the case of the brown dwarf EB, the models do seem to be reasonably consistent with both objects, but the secondary appears to be hotter than the primary, a very surprising result that was not predicted by any of the models.

The study of low-mass stars poses a challenge for stellar models. Stars near to the hydrogen-burning limit are sufficiently cool that the interior is in a partially degenerate state on the main-sequence (Chabrier & Baraffe 1997), and magnetic fields may play an important role (Mullan & MacDonald 2001). The approximations underlying the usual 'grey' atmosphere models break down, so non-grey model atmospheres must be determined, taking account of effects such as the recombination of molecules (e.g. H_2 and TiO) due to the low temperatures (Baraffe et al. 2002). One of the ways to test these models is by comparison with precise observations of low-mass stars.

It is therefore essential that a larger sample of PMS systems be found and characterized to provide better constraints on the models. This is the primary aim of the Monitor project (Hodgkin et al. 2006; Aigrain et al. 2007), a photometric monitoring survey we have undertaken of all suitable nearby, PMS open clusters and star-forming regions, to search for detached EB and transiting planet systems. This publication presents the first of these, a detached EB in the ONC, which has age 1 ± 1 Myr and distance $\sim$470 pc (Hillenbrand 1997).

Sections 2 and 3 review the photometric and spectroscopic observations and analysis, respectively. Section 4 presents the light-curve analysis and system parameters, and in Section 5 these are compared with the predictions of stellar models. Finally, we summarize our conclusions in Section 6.

2 PHOTOMETRY

2.1 Survey photometry

Eclipses in JW 380 were initially detected in our photometric monitoring data of the ONC obtained using the 2.5 m Isaac Newton Telescope (INT), with the Wide Field Camera (WFC), during two 10-night observing runs, one in 2004 late-November, and one in 2005 January. This was supplemented by two further 10-night runs in 2005 December and 2006 December.

A single $\sim$34 × 34-arcmin^2 field centred on the trapezium region (θ_C^1 Ori) was observed for the entire time it was at airmass <2.0,

$\sim$6 h per night, using alternating 60 s *V*-band and 30 s *i*-band exposures. Due to the fast ($\sim$40−45 s) readout of the WFC this gave a cadence of $\sim$3.5 min. A total of 1400 exposures were obtained in each passband, for a total time on target of $\sim$80 h. Our observations are sufficient to give an rms per data point of 1 per cent or better down to $i \sim 17$ and $V \sim 18$.

Light curves were extracted for a total of 2500 objects using our differential photometry software (Irwin et al. 2007). The *V*-band light curves in particular are somewhat affected by the presence of nebulosity in the ONC region, and show significantly more scatter than the *i*-band data. We therefore used the latter for detection of EB systems, and the *V*-band observations for confirmation.

Due to the extensive intrinsic stellar variability seen in ONC stars (e.g. Stassun et al. 1999; Herbst et al. 2002), the search for eclipsing systems was by necessity performed manually. The first candidate detected in this way is the subject of the present paper. The *i*-band light curve (see the upper panel of Fig. 1) shows $\sim$0.05-mag eclipse events, with $\sim$0.03-mag peak-to-peak out-of-eclipse variations.

The object appears in the catalogue of Jones & Walker (1988) as star 380, with membership probability 0.99 derived from proper motion measurements by these authors. It was also detected by the *Chandra* Orion Ultradeep Project (COUP; Getman et al. 2005, star 468), and in the Two Micron All Sky Survey (2MASS), as source 2MASS J05351214−0531388.

The photometric properties of the object are summarized in Table 1. *V* and *I* magnitudes were derived from the Monitor photometry using colour equations from the INT wide-field survey web pages,[1] and the near-infrared *J*, *H* and *K* magnitudes from the 2MASS photometry using colour equations in the 2MASS explanatory supplement.[2] *Spitzer*/IRAC measurements are from table 1 of Rebull et al. (2006).

The measured composite *I*-band magnitude and the models of Baraffe et al. (1998) imply a total system mass of $\sim$0.5 $M_\odot$ if the system was a single star, or assuming that the primary contributes half of the system light, $\sim$0.3 $M_\odot$ (the latter is a more reasonable assumption for a near equal-mass binary), and the optical colour $V − I = 3.1$ implies a spectral type of $\sim$ M5 using the intrinsic colours of Leggett (1992).

---

[1] http://www.ast.cam.ac.uk/~wfcsur/technical/photom/colours/.
[2] http://www.ipac.caltech.edu/2mass/releases/allsky/doc/sec6_4b.html.

Table 1. Photometric properties of the EB system. Errors are not quoted for the INT/WFC photometry because these are dominated by systematic errors from the sky subtraction due to the extensive nebulosity in the optical. We expect that these are <0.05 mag.

Passband	Magnitude	Source
V_J	16.92	INT/WFC
I_C	13.82	INT/WFC
J_{CIT}	12.13 ± 0.02	2MASS
H_{CIT}	11.42 ± 0.03	2MASS
K_{CIT}	11.14 ± 0.02	2MASS
[3.6]	10.86 ± 0.005	*Spitzer*/IRAC
[4.5]	10.80 ± 0.005	*Spitzer*/IRAC
[5.8]	10.72 ± 0.033	*Spitzer*/IRAC
[8.0]	10.04 ± 0.086	*Spitzer*/IRAC

Passbands	Colour	Source
$V_J - I_C$	3.10	INT/WFC
$J_{CIT} - H_{CIT}$	0.71 ± 0.04	2MASS
$H_{CIT} - K_{CIT}$	0.28 ± 0.04	2MASS
[3.6] − [4.5]	0.06 ± 0.007	*Spitzer*/IRAC
[4.5] − [8.0]	0.76 ± 0.086	*Spitzer*/IRAC

Examination of the COUP light curve[3] shows two flare events, but no obvious evidence for eclipses at the present time. This is under investigation, in collaboration with members of the COUP team.

Spitzer/IRAC measurements for JW 380 are available in table 1 of Rebull et al. (2006), and are reproduced here in Table 1. Comparing the observed [3.6]–[4.5] and [4.5]–[8.0] colours to those derived in NGC 2362 by Dahm & Hillenbrand (2007) indicates that these measurements may provide evidence for a weak disc excess, but this conclusion is somewhat ambiguous due to the obvious composite nature of the system, which will affect the observed colours.

From the full INT/WFC data set, a preliminary period of 2.65 d was determined using a standard box-fitting least-squares transit search program (Aigrain & Irwin 2004).

2.2 Follow-up photometry

Initial follow-up observations were obtained during 2006 February by J. Holtzman using the New Mexico State University 1.0 m robotic telescope, in *I* band, at the predicted times of eclipse from the INT data.

JW 380 was also monitored using the 0.9, 1.0 and 1.3 m telescopes[4] at the Cerro Tololo Inter-American Observatory. Observations were obtained from 2005 December to 2007 January, in *V* and *I* bands, although the majority of the data are in *I* band. Differential light curves were determined from point spread function fitting photometry using an algorithm for inhomogeneous ensemble photometry (Honeycutt 1992) as implemented in Stassun et al. (1999, 2002) for observations of high-nebulosity regions such as the ONC.

All the available data were combined to produce two composite light curves, one in *I* band and the other in *V* band, applying a normalization to account for zero-point offsets between the various photometric systems in use, based on the median out-of-eclipse level. Note that the *i* and *I* passbands are not strictly identical: the *i* [Sloan Digital Sky Survey (SDSS)] passband is slightly bluer than

the conventional *I* (Cousins) passband, by ∼10 per cent in the *V* − *I* colour. However, with the present data it is difficult to correct for this effect, and we expect that the errors introduced by not doing so will be negligible given the photometric errors.

An updated period of 2.6496 d was determined by applying a new double trapezoid fitting program (Aigrain et al., in preparation).

2.3 Out-of-eclipse variations

The out-of-eclipse variations were found not to phase-fold at the same period as the EB, and moreover with the full combined data set it was not possible to find a consistent period for them, presumably due to changes in the spot coverage of the stellar surfaces causing phase and amplitude changes in the out-of-eclipse modulations, over shorter time-scales than the observing window.

The INT/WFC data considered alone are concentrated into $4 \times \sim 10$ night observing runs, so we attempted fitting of the out-of-eclipse parts of this light curve. If these are due to spots on the surface of one of the component stars, this allows the rotation period of the star to be determined, and if a sufficiently good model for the spot behaviour can be found, the modulations can be removed, to improve the accuracy of the EB model fit.

The period-finding algorithm from Irwin et al. (2006) (based on least-squares fitting of sinusoidal modulations) was modified to fit different phases, amplitudes and zero-point levels for each of the four observing runs, fitting for a common period, presumed to be the rotation period of the star. The results of this procedure are shown in Fig. 2.

Fig. 2 indicates that the fit provides a good description of the majority of the out-of-eclipse variations, except in the first five nights and the penultimate night. This indicates that a model assuming a constant stellar rotation period, here 4.9 d (which is not equal to the binary period or a multiple thereof), and with moderate evolution of spot coverage over one month time-scales, provides a good description of the majority of the out-of-eclipse variability. We note also that Herbst et al. (2002) list a rotation period of 4.75 d for this star, which tends to confirm our result.

However, Fig. 2 shows that the model we have presented does not completely describe the variation in the nights containing eclipses, and this technique is not applicable to the follow-up data due to the sparse time coverage (providing insufficient data to fit the rotational modulations in each individual light-curve segment, before the spot configuration changes).

Therefore, we elected to simply reduce the effect of the out-of-eclipse variability on the measured eclipse depths by subtracting the median out-of-eclipse light-curve level from each night containing an eclipse (see the lower panel of Fig. 1), since this technique treats the entire composite light curve consistently. We caution that this is *not* equivalent to modelling the spots physically, which will be necessary for a more accurate light-curve fit to improve the derived physical parameter estimates. Fortunately, in most cases the effect of the spots on the inferred physical parameters is minor. For example, in the analysis of the young EB V1174 Ori, Stassun et al. (2004) found that modelling the out-of-eclipse variability with spots did not alter the derived stellar parameters significantly, with changes of <1 per cent in the derived masses and radii, and <3 per cent in the ratio of effective temperatures.

3 SPECTROSCOPY

In order to confirm the EB nature of the system, and to derive the orbital parameters, multiple radial velocity measurements are

---

[3] Light curves are available in the source atlas on the COUP web site: http://www.astro.psu.edu/coup/.
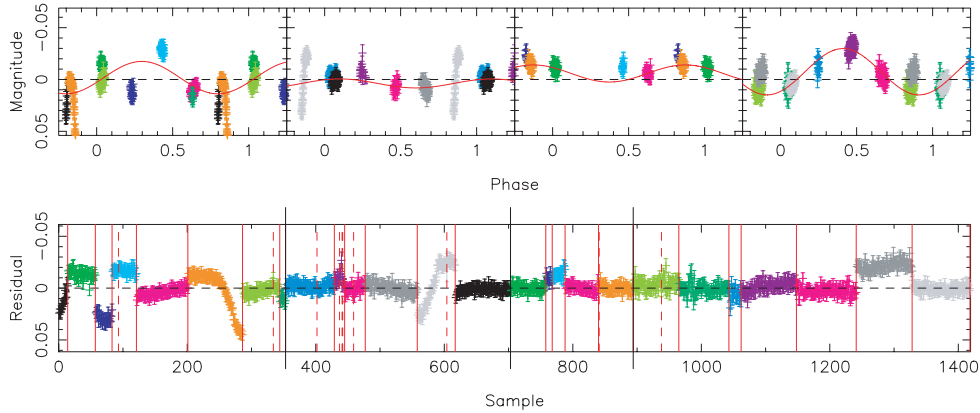[4] Now operated by the SMARTS consortium.

Figure 2. Fitting of the INT/WFC *i*-band light-curve out-of-eclipse variations. The upper panels show the phase-folded light curve for each of the four observing runs, fit with the same period, but a different phase, amplitude and zero-point in each, with the fit overlaid as a solid line. The lower panel shows the residuals after subtracting the fit, plotted as a function of sample number. The dashed horizontal lines show the median light-curve level. The vertical lines in the lower plot show the boundaries between nights of observations, with the boundaries between observing runs (corresponding to the division of the panels in the upper plot) denoted by longer black vertical lines.

required. These were obtained using two instruments: the FLAMES multi-object fibre-fed échelle spectrograph on VLT UT2 in the optical, and the NOAO Phoenix spectrograph on Gemini South.

3.1 VLT/FLAMES

VLT/FLAMES observations were obtained during 2006 November (programme 078.C-0841). GIRAFFE fibres were allocated to all of our EB candidates in addition to 220 other suspected ONC members. A total of five spectra were obtained in each of two standard settings: HR15n covering $\sim 6450-6810$ Å with resolving power $R \sim 17\,000$ and HR21 covering $\sim 8490-8980$ Å at $R \sim 16\,000$. Data were reduced using the GIRAFFE Base-Line Data Reduction Software (Blecha et al. 2000), with additional custom-written software for sky subtraction using 13 fibres allocated to blank sky. The HR15n setting was strongly contaminated by spatially variable emission lines from the Orion nebula, so we preferred the HR21 setting for determination of radial velocities, and this has been used henceforth.

Radial velocities were determined by cross-correlation using FX-COR in IRAF[5] (Tody 1993). Since it is impractical to observe radial velocity standard stars with FLAMES, we used model atmosphere spectra from the $R \sim 20\,000$ MARCS library (Gustafsson et al. 2003) to provide the cross-correlation templates. Cross-correlations for the present object were derived using a template with $T_{\mathrm{eff}} = 3500$ K, solar metallicity, and $\log g = 3.5$, in accordance with the predicted surface gravity from the 1 Myr stellar models of Baraffe et al. (1998). Radial velocity errors were estimated using the method of Tonry & Davis (1979) as implemented in FXCOR.

The observed cross-correlation functions show clear triple-lined profiles (see Fig. 3) in a total of seven epochs (including also the Gemini/Phoenix data, see Section 3.2) around maximum radial velocity separation, with the two outer components (the primary and
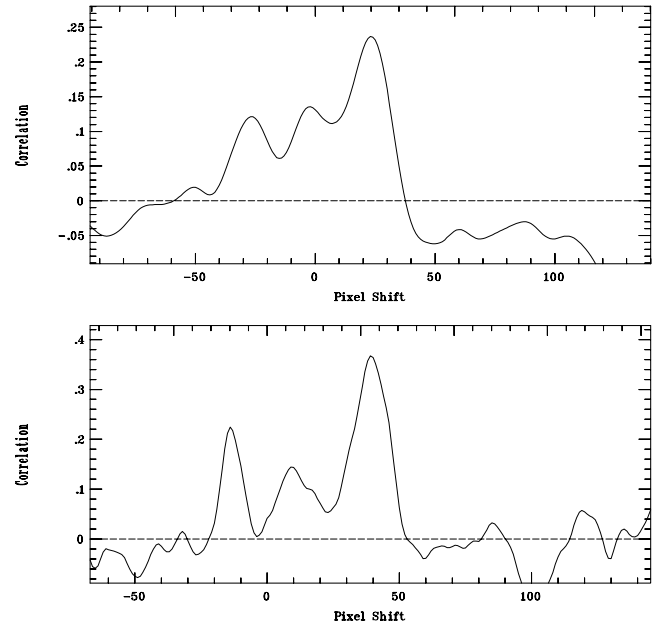
Figure 3. Cross-correlation function for the first VLT/FLAMES spectrum (top), and a Gemini/Phoenix spectrum for comparison (bottom, see also Section 3.2), showing a clear triple-lined profile in both cases. The central component does not appear to show significant radial velocity variations. A three-component Gaussian fit was used to determine the radial velocities, with cross-correlation peak heights (left- to right-hand side) 0.11, 0.12, 0.23 in the VLT/FLAMES spectrum.

secondary stars in the EB) exhibiting radial velocity variations. The central component (hereafter the tertiary – although note that this star is not necessarily physically associated with the binary) does not appear to show radial velocity variations.

We note that strong Li I 6707.8-Å absorption is clearly visible in the HR15n setting, which indicates youth, and hence membership of the ONC. The lithium line profiles from our five HR15n spectra are shown in Fig. 4. Equivalent widths were estimated by fitting

in our spectra (e.g. Ni I 6643 Å, Fe I 6663 Å or V I 6625 Å as used by Palla et al. 2007) with which to compute the veiling, despite the majority of our spectra having very good signal-to-noise ratios ($\sim$40 pix^{-1} or 180 Å^{-1}). The values we have computed must therefore be considered to give lower limits on the measured lithium abundance. Nevertheless, assuming the primary to contribute half of the light in the system, the implied equivalent width is $\sim$0.6 Å, which is a typical value for ONC stars of this mass (e.g. see Sicilia-Aguilar et al. 2005).

3.2 Gemini/Phoenix

Additional radial velocity measurements were obtained using the near-infrared spectrograph Phoenix (Hinkle et al. 2002) on Gemini South, on three nights: 2006 December 1, 2 and 4 (programme GS-2006B-C-7). Following Mazeh et al. (2002), we used the H6420 order-sorting filter and the widest (4 pix $\approx$ 0.34 arcsec) slit, with a central wavelength of 1.558 μm to give a wavelength range of $1.554 - 1.562$ μm at resolving power $R \sim 35\,000$. Exposures were taken in *AB* pairs, nodding along the slit, to aid subtraction of the sky background and residual dark current features in the detector. A total of eight epochs were obtained for this object, with average signal-to-noise ratios of $\sim$60 pix^{-1} or 220 Å^{-1}. Data were reduced using standard IRAF long-slit reduction procedures, and cross-correlations with the radial velocity standard star GJ 173 (M1.5 spectral type) in FXCOR were used to derive radial velocities, since this template gave the largest cross-correlation signal. This suggests that the primary spectral type is close to M1.5. Using the effective temperature scale of Cohen & Kuhi (1979), this corresponds to $T_{\mathrm{eff}} = 3590$ K.

Despite the high resolution and high signal-to-noise ratio of our data, it is difficult to see the individual line profiles in the Phoenix spectra. This may be partly due to the very strong dependence on spectral type in this wavelength region (e.g. see Bender et al. 2005), where the atomic lines become weak moving to the later spectral type secondary and tertiary components. This also partly explains the reduction in cross-correlation signal for these objects (see Fig. 3), since we used an earlier type template with strong atomic lines.

We note that the unavoidable use of different templates for the two instruments may introduce systematic offsets between the two sets of radial velocities. We have tried to minimize this source of error by using templates with similar effective temperatures.

3.3 Spectroscopic orbit solution

The photometry and initial VLT/FLAMES radial velocities were found to be consistent with the photometrically derived period, but the Gemini/Phoenix velocities were not. A consistent solution was found at twice the initial period, or 5.2991 d. Re-examination of the light curve indicated that three secondary eclipses had in fact been observed, and that these had depths of $\sim$0.03 mag in *i* band. This is simply a result of the improved phase coverage obtained by including the Gemini/Phoenix radial velocity data.

Fig. 5 shows the resulting phase-folded radial velocity curve, with period and phase zero-point fixed at the photometrically determined values. Neither the light curve nor radial velocity curve appears to show significant deviation from the predictions for a circular orbit, with a formal fit giving eccentricity $e = 0.004 \pm 0.036$, so we have assumed zero eccentricity henceforth.

Table 2 gives the orbital parameters derived from the radial velocity fit.

The measured systemic velocity (v_{sys}) is 26.55 ± 0.87 km s^{-1}. This is very close to the systemic velocity of the ONC, of 25 $\pm$

Figure 4. Lithium 6707.8-Å line profiles for the five VLT/FLAMES spectra in the HR15n setting. Arrows show the predicted positions of the lines from the three components (1, 2 and 3 are primary, secondary and tertiary, respectively), derived from the radial velocities. The primary and secondary show clear lithium absorption, and the tertiary may also show it, but this line, if present, is not well resolved from the primary in any of the spectra.

three-component Gaussian models to the two best resolved epochs (the first and third in Fig. 4), at the expected wavelengths from the radial velocities for each component. The values obtained were 0.32 ± 0.05 Å for the primary, 0.18 ± 0.04 Å for the secondary, and 0.12 ± 0.05 Å for the tertiary (errors estimated using bootstrapping). Note that in order to compare to the values for single stars, these measured equivalent widths must be corrected for the relative luminosities of the stars.

Unfortunately, we are unable to correct the Li I equivalent widths for spectral veiling at present, since we do not see suitable features
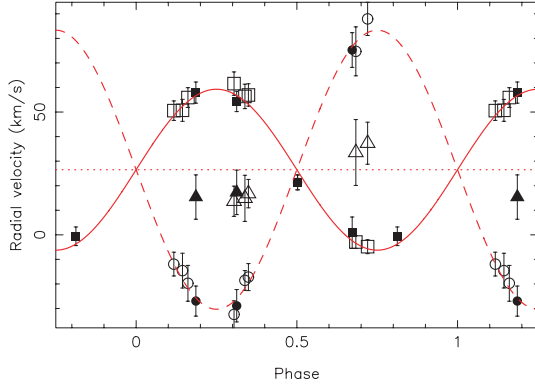
Figure 5. Radial velocity curve, folded on a period of 5.2991 d, where phases 0, 1, . . . are defined to be at mid-secondary eclipse. The curves show the fit for a circular orbit, to the primary (solid line) and secondary (dashed line) radial velocities. The dotted line indicates the systemic radial velocity. Points with error bars show the radial velocity measurements for all three components of the system (primary: squares, secondary: circles, tertiary: triangles), filled symbols denote radial velocity points from VLT/FLAMES, and open symbols points from Gemini/Phoenix. Velocities for the system components were only measured when the corresponding peaks were visible in the cross-correlation functions, so some data points are missing for the secondary and tertiary components, particularly close to phases 0 and 0.5. The tertiary velocities are poorly measured and are strongly influenced by blending of the cross-correlation profiles (e.g. see Fig. 3), so the apparent variations for this component are not considered significant in the present data.

Table 2. System parameters derived from the radial velocity curve fit in Fig. 5.

Systemic velocity	v_{sys}	$26.55 \pm 0.87 \, \mathrm{km \, s^{-1}}$
Primary semi-amplitude	K_1	$32.8 \pm 1.3 \, \mathrm{km \, s^{-1}}$
Secondary semi-amplitude	K_2	$56.9 \pm 2.2 \, \mathrm{km \, s^{-1}}$
Mass ratio (M_2/M_1)	q	0.577 ± 0.032
Semimajor axis	$a \sin i$	$9.38 \pm 0.27 \, \mathrm{R_\odot}$
Total mass	$M \sin^3 i$	$0.396 \pm 0.019 \, \mathrm{M_\odot}$
Primary mass	$M_1 \sin^3 i$	$0.251 \pm 0.023 \, \mathrm{M_\odot}$
Secondary mass	$M_2 \sin^3 i$	$0.145 \pm 0.012 \, \mathrm{M_\odot}$
Reduced χ^2	χ^2_ν	0.60

$1.5 \, \mathrm{km \, s^{-1}}$ (Stassun et al. 1999; Sicilia-Aguilar et al. 2005), which provides a further kinematic confirmation of cluster membership.

Since the tertiary lies approximately at the ONC systemic velocity in the cross-correlations, it seems likely that this star is also a member of the ONC. If this is the case, the measured stellar density in the ONC (e.g. Hillenbrand 1997 found ~1600 members with $I < 17.5$ over a 0.2-deg² region) indicates a probability of ~10^{-4} of a chance superposition of another ONC member with the binary, within 0.5 arcsec (the best seeing experienced in our observing runs). It thus seems likely that the system is a physical triple.

4 LIGHT-CURVE ANALYSIS

The *i*-band light curve was analysed using JKTEBOP (Southworth, Maxted & Smalley 2004a; Southworth et al. 2004b), a modified version of EBOP (Eclipsing Binary Orbit Program; Popper & Etzel

1981; Etzel 1981). These codes use a model in which the discs of the stars are approximated using biaxial ellipsoids (Nelson & Davis 1972). This approximation is only applicable in well-detached systems where the stars are close to spherical, as in the present case. Note that star spot modelling and handling of multiband light curves are not implemented in these codes, and must be done externally, as we have in the present work. The JKTEBOP code contains several enhancements, including fitting of the sum and ratio of the stellar radii, the use of the Levenberg–Marquardt minimization algorithm for least-squares fitting (Press et al. 1992), and of particular interest for the present discussion, Monte Carlo simulation to determine robust error estimates for the stellar parameters, which has been shown to give reliable results (Southworth et al. 2005). Note that we have not used the *V*-band light curve in the present analysis, since there are no secondary eclipses observed, and the photometric precision reached is somewhat poorer. The observed primary eclipses have very similar depth to the *i*-band eclipses.

The light-curve analysis for the present system is complicated by the known presence of third light. From Fig. 3, it appears that the
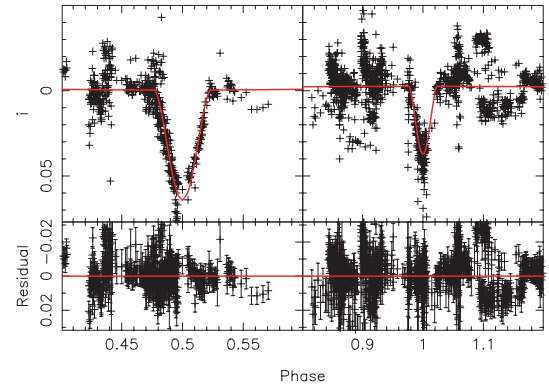

Figure 6. Phase-folded combined *i*-band light curve, with phase 0 defined to be at mid-secondary eclipse, as Fig. 5. The upper panel shows the light curve, with the fit overlaid (solid line), and the lower panel shows the residuals (data − model). The panels show a magnified view of the regions around primary eclipse (left-hand panels) and secondary eclipse (right-hand panels). The scatter in the secondary eclipse is larger than the primary since this was only observed in the follow-up observations and not the INT/WFC survey photometry (which was of better photometric precision).

Table 3. System parameters derived from the light-curve fit in Fig. 6. Note that J, L_3 and L_2/L_1 are the quantities for *i* band. 68 per cent confidence intervals are quoted. Note that since the effective temperatures are unknown, the temperature ratio was calculated assuming equal bolometric corrections for both components.

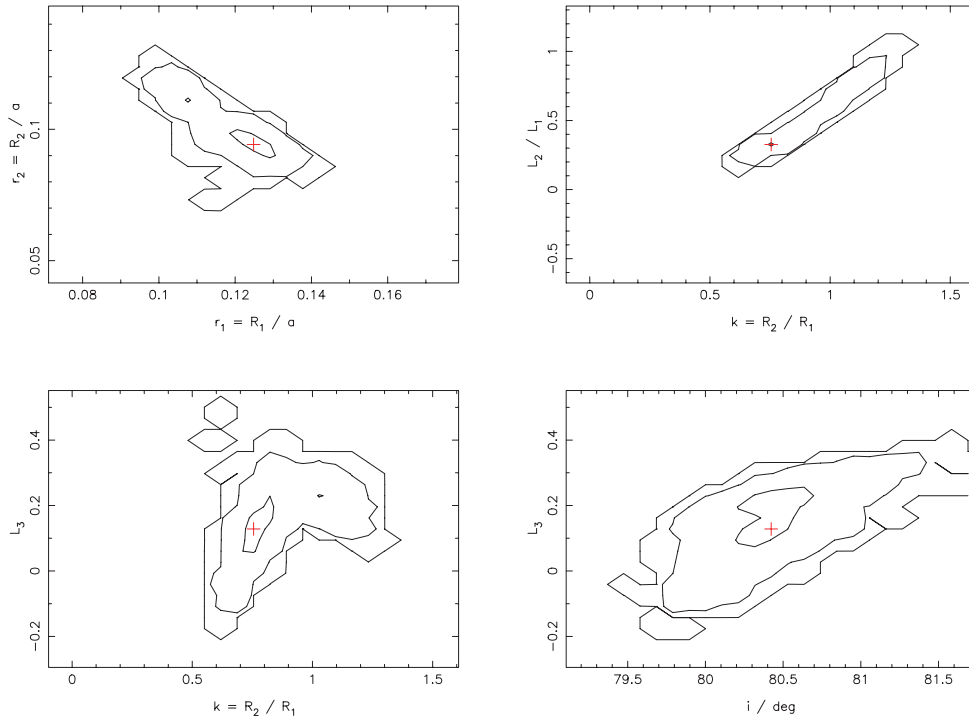|		
Radius sum	$(R_1 + R_2)/a$	$0.2191^{+0.0035}_{-0.0039}$
Radius ratio	k	$0.75^{+0.30}_{-0.04}$
Orbital inclination	i	$80°.42^{+0°.27}_{-0°.26}$
Surface brightness ratio	J	$0.573^{+0.045}_{-0.011}$
Third light ratio	L_3	$0.128^{+0.111}_{-0.058}$
Orbital period	P	$5.299\,180^{+0.000\,013}_{-0.000\,014}$ d
Phase zero-point (HJD)	T_0	$2449\,704.452\,79^{+0.009\,98}_{-0.009\,46}$
Primary radius	R_1/a	$0.1248^{+0.0031}_{-0.0184}$
Secondary radius	R_2/a	$0.0942^{+0.0182}_{-0.0029}$
Luminosity ratio	L_2/L_1	$0.3265^{+0.3635}_{-0.0372}$
Temperature ratio	T_2/T_1	$0.8700^{+0.0168}_{-0.0041}$

Figure 7. Confidence intervals on the light-curve fitting parameters from the Monte Carlo simulations. The contours show the 68.3, 95.4 and 99.73 per cent confidence levels, corresponding to 1, 2 and 3σ standard errors. The crosses indicate the best-fitting values. The panels show: r_2 versus r_1 (top left-hand panel), luminosity ratio L_2/L_1 versus radius ratio k, fractional third light luminosity L_3 versus k and L_3 versus orbital inclination i. Degeneracies between r_1 and r_2, and L_2/L_1 and k (due to the existence of solutions for $k < 1$ and for $k > 1$ as discussed in the text) are clearly visible. Note that the 3σ contours are likely to be underestimated due to the limited number of Monte Carlo samples used.

cross-correlation peaks for the secondary and tertiary are of very similar height and shape, which suggests that the third light star has a similar flux and spectral type to the secondary. We therefore expect it to contribute $\sim 1/4$ of the light in the system, assuming a 2:1:1 ratio of i-band luminosity.

Due to the need to fit the third light contribution, we fixed as many parameters as possible, to improve stability. In I band, limb darkening is of much lower importance than for bluer passbands, so we fixed these parameters. We used a linear limb-darkening law:

$$\frac{I_\lambda(\mu)}{I_\lambda(1)} = 1 - x_\lambda(1 - \mu), \tag{1}$$

where $\mu = \cos\theta$ is the cosine of the angle between the line of sight and the normal to the stellar surface, $I_\lambda(\mu)$ is the observed surface intensity at wavelength λ as a function of μ, and x_λ is the linear limb-darkening coefficient. Values of x_λ of 0.7208 for the primary star ($T_{\rm eff} = 3300\,{\rm K}$, $\log g = 4.0$, [M/H] $= 0$) and 0.7341

Table 4. Physical parameters derived from the combined radial velocity and light-curve fitting. Note that the errors on M_1 and M_2, and R_1 and R_2 are not independent since they are calculated from the mass ratio and radius ratio.

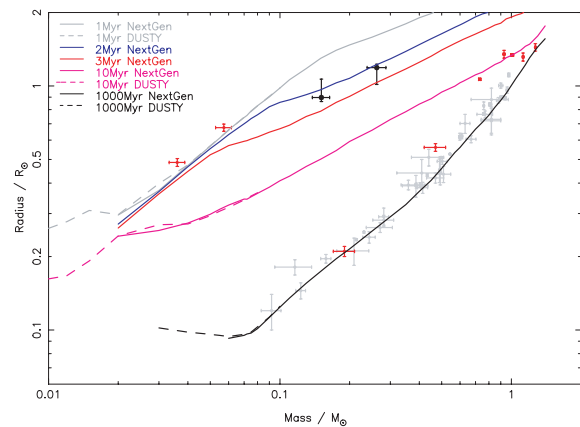|		
Primary mass	M_1	$0.262^{+0.025}_{-0.024}\,{\rm M_\odot}$
Secondary mass	M_2	$0.151^{+0.013}_{-0.013}\,{\rm M_\odot}$
Primary radius	R_1	$1.189^{+0.039}_{-0.175}\,{\rm R_\odot}$
Secondary radius	R_2	$0.897^{+0.170}_{-0.034}\,{\rm R_\odot}$
Semimajor axis	a	$9.52^{+0.27}_{-0.27}\,{\rm R_\odot}$
Primary gravity	$\log(g_1)$	$3.706^{+0.137}_{-0.025}\,{\rm cm\,s^{-1}}$
Secondary gravity	$\log(g_2)$	$3.711^{+0.029}_{-0.155}\,{\rm cm\,s^{-1}}$

Figure 8. Mass–radius relation for low-mass stars and EBs. The present system is shown by the black points with error bars, and the lines show PMS NextGen ($\alpha = 1.0$, solid lines; Baraffe et al. 1998) and DUSTY (dashed lines; Chabrier et al. 2000) models from the Lyon group, at five ages (top to bottom): 1 Myr (grey line), 2 Myr (blue), 3 Myr (red), 10 Myr (magenta) and 1 Gyr (black). Systems shown as red points with error bars are existing PMS binaries from Covino et al. (2001, 2004), Stassun et al. (2004), Hebb et al. (2006) and Stassun et al. (2007). The small grey points with error bars are a compilation of field systems from Delfosse et al. (2000), Lane, Boden & Kulkarni (2001), Ségransan et al. (2003), Lopez-Morales (2004), Bouchy et al. (2005), Pont et al. (2005) and Lopez-Morales et al. (2006). We have opted to show results from the literature to produce a figure summarizing the present empirical constraints on the PMS mass–radius relation. The DUSTY models are included to show the predicted behaviour in the brown dwarf domain.
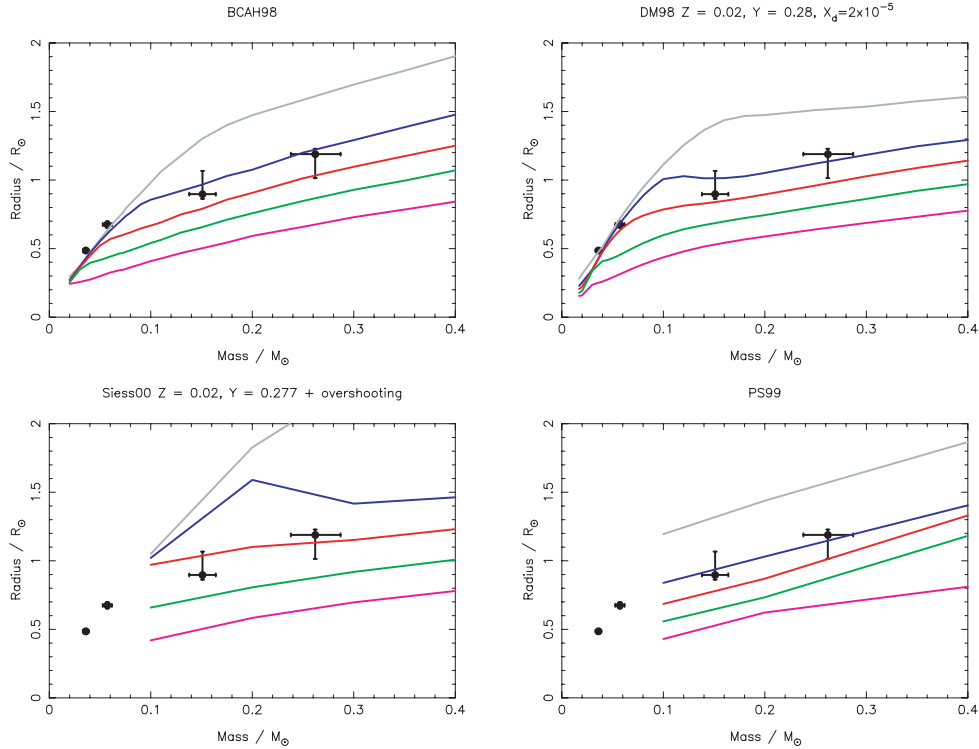
Figure 9. Comparison of the EB system with several models of low-mass stars. The EB data are shown by the black points with error bars, and the lines show PMS models for (top to bottom): 1 Myr (grey line), 2 Myr (blue), 3 Myr (red), 5 Myr (green) and 10 Myr (magenta). Top left-hand panel: Baraffe et al. (1998) for solar metallicity and $\alpha = 1.0$; top right-hand panel: D'Antona & Mazzitelli (1998) for $Z = 0.02$, $Y = 0.28$, $X_d = 2 \times 10^{-5}$; bottom left-hand panel: Siess et al. (2000) for $Z = 0.02$, $Y = 0.277$, with (moderate) convective overshooting; bottom right-hand panel: Palla & Stahler (1999). The models have been interpolated where necessary to provide points at the required ages. The brown dwarf EB system of Stassun et al. (2006) (using the parameters from Stassun et al. 2007) is shown to allow the inferred ages to be compared, since this is suspected to also be a member of the ONC, and should therefore be assigned a similar age to JW 380. Note that the Siess et al. (2000) and Palla & Stahler (1999) models do not provide points below $0.1\,M_{\odot}$.

($T_{\rm eff} = 3100$ K, $\log g = 4.0$, $[{\rm M/H}] = 0$) for the secondary star were adopted from Claret (2004), for the SDSS $i\prime$ passband, which is the closest match to the SDSS-like i filters used in this work. The gravity-darkening exponents were also fixed, at $\beta = 0.08$, a value appropriate for stars with convective envelopes (Lucy 1967), and the option in JKTEBOP to calculate the reflection effect was used, rather than fitting for it. This is generally a reasonable approach for well-detached systems.

The remaining parameters were allowed to vary. These are the sum of the radii, $r_1 + r_2$ (where $r_i = R_i/a$, the radius divided by semimajor axis, a parameter which can be determined from the light-curve analysis alone), the radius ratio $k = r_2/r_1$, orbital inclination i, surface brightness ratio J (again defined as secondary divided by primary such that $J \leqslant 1$) and fractional luminosity of the third light L_3. We also allowed the period P and phase zero-point T_0 (defined as the heliocentric Julian Day of the secondary eclipses) to vary, to refine the existing values. Note that the quantity J and the luminosities quoted here are for i band.

Note that the EBOP codes model only single-band light curves, and do not use model atmospheres, so it is not necessary to assume an effective temperature or surface gravity in the fit itself: these parameters enter only through the (assumed) limb-darkening coefficients, and we expect this dependence to be weak in i band.

Fig. 6 show the i-band phase-folded light curve, with the fit overlaid. The system parameters derived from the light-curve fitting are given in Table 3. Errors were estimated using the Monte Carlo analysis, with 10 000 iterations, the results of which are also shown in Fig. 7.

The Monte Carlo algorithm uses the best fit to generate a synthetic light curve, injecting Gaussian noise with amplitude determined by the observational errors to produce a simulated light curve, which is then fitted to determine a new set of parameters. The errors can be estimated using the distribution of the parameters from a large number of realizations of this process. See also Southworth et al. (2004a) and Southworth et al. (2004b) for more details.

Since the luminosity ratio was not constrained in the analysis, the solution with the radii of the two stars swapped ($k > 1$ or $R_2 > R_1$) is also formally permitted by the fit, which leads to highly asymmetric errors for k, L_2/L_1 and the two fractional radii.

Table 4 summarizes the final system parameters, combining the radial velocity and light-curve information. Note the extremely large stellar radii and low surface gravities, as expected for a very young system.

We caution that the effects of the out-of-eclipse modulations are non-negligible in this system, and these have not been modelled at present due to the lack of suitable light-curve data. Therefore, the parameters derived from the light-curve fitting may be affected by systematic errors due to not properly accounting for the spot-induced photometric variations. Improved light curves will be required to resolve this problem.

5 COMPARISON WITH STELLAR MODELS

We are unable to determine accurate effective temperatures at the present time, so the only comparison which can be made to stellar models with the present data set is in the mass–radius plane. Fig. 8

shows a comparison of the observations for the present system with the Lyon group stellar models. The primary and secondary are consistent within the 1σ error bars with the 2 Myr model of Baraffe et al. (1998), but ∼2σ away from the 1 Myr model. The primary is also consistent within 1σ with the 3 Myr model. The value of 2 Myr is fully consistent with the upper end of the canonical 1 ± 1 Myr age for the ONC (Hillenbrand 1997).

Fig. 9 shows the position of the EB relative to models from Baraffe et al. (1998), D'Antona & Mazzitelli (1998), Siess, Dufour & Forestini (2000) and Palla & Stahler (1999). The results for the Baraffe et al. (1998), D'Antona & Mazzitelli (1998) and Palla & Stahler (1999) are consistent with the 2 Myr inferred age from above; although there are clearly visible differences between the results of these sets of tracks (especially when comparing D'Antona & Mazzitelli 1998 to the others), the measurement errors are too large to distinguish them at present. Comparing the data with the models of Siess et al. (2000) would indicate a slightly older age of ∼3 Myr. However, there is a visible discontinuity in the latter tracks at 2 Myr, and they are not well sampled over this mass range.

Given the present observational errors, it is not yet meaningful to perform a more detailed comparison with stellar models. We plan to obtain improved photometry and radial velocity measurements to resolve this, in addition to spectroscopy covering suitable lines for determining effective temperatures and flux ratios.

6 CONCLUSIONS

We have reported the detection of a new PMS EB, JW 380, which appears to be a member of the ONC (membership probability 0.99, systemic velocity within 1σ of the cluster systemic velocity). The system consists of a 0.26 ± 0.02, $0.15 \pm 0.01\,\mathrm{M}_\odot$ EB with period $5.299\,180 \pm 0.000\,013$ d, blended with a significant (∼20 per cent of the total luminosity) third light component, which appears to show no significant radial velocity variations over the (limited) observing window.

Modelling the combined light and radial velocity curves for the system yielded stellar radii of $1.19^{+0.04}_{-0.18}$ and $0.90^{+0.17}_{-0.03}\,\mathrm{R}_\odot$ for the primary and secondary of the binary system. These large radii are consistent with the 2 Myr age stellar models of Baraffe et al. (1998), D'Antona & Mazzitelli (1998) and Palla & Stahler (1999), and the 3 Myr age models of Siess et al. (2000) given the masses of the system components. The systemic radial velocity is consistent with that of the ONC, and the detection of a clear Li I 6707.8-Å absorption feature is also suggestive of youth, and hence ONC membership.

REFERENCES

Aigrain S., Irwin M., 2004, MNRAS, 350, 331
Aigrain S., Hodgkin S., Irwin J., Hebb L., Irwin M., Favata F., Moraux E., Pont F., 2007, MNRAS, 375, 29
Baraffe I., Chabrier G., Allard F., Hauschildt P. H., 1998, A&A, 337, 403
Baraffe I., Chabrier G., Allard F., Hauschildt P. H., 2002, A&A, 382, 563
Bender C., Simon M., Prato L., Mazeh T., Zucker S., 2005, AJ, 129, 402
Blecha A., Cayatte V., North P., Royer F., Simond G., 2000, in Iye M., Moorwood A. F., eds, Proc. SPIE Vol. 4008, Optical and IR Telescope Instrumentation and Detectors. SPIE, Bellingham WA, p. 467
Bouchy F., Pont F., Melo C., Santos N.C., Mayor M., Queloz D., Udry S., 2005, A&A, 431, 1105
Burrows A. et al., 1997, ApJ, 491, 856
Chabrier G., Baraffe I., 1997, A&A, 327, 1039
Chabrier G., Baraffe I., Allard F., Hauschildt P., 2000, ApJ, 542, 464
Claret A., 2004, A&A, 428, 1001
Cohen M., Kuhi L. V., 1979, ApJS, 41, 743
Covino E., Melo C., Alcalá J. M., Torres G., Fernández M., Frasca A., Paladino R., 2001, A&A, 375, 130
Covino E., Frasca A., Alcalá J. M., Paladino R., Sterzik M. F., 2004, A&A, 427, 637
Dahm S. E., Hillenbrand L., 2007, AJ, 133, 2072
D'Antona F., Mazzitelli I., 1997, Mem. Soc. Astron. Ital., 68, 807
D'Antona F., Mazzitelli I., 1998, in Rebolo R., Martin E. L., Zapatero Osorio M. R., eds, ASP Conf. Ser. Vol. 134, Brown Dwarfs and Extrasolar Planets. Astron. Soc. Pac., San Francisco, p. 442
Delfosse X., Forveille T., Ségransan D., Beuzit J.-L., Udry S., Perrier C., Mayor M., 2000, A&A, 364, 217
Etzel P. B., 1981, in Carling E. B., Kopal Z., eds, NATO ASI Ser. C Vol. 69, Photometric and Spectroscopic Binary Systems. Kluwer, Dordrecht, p. 111
Getman K. V. et al., 2005, ApJS, 160, 319
Girardi L., Bressan A., Bertelli G., Chiosi C., 2000, A&AS, 141, 371
Gustafsson B., Edvardsson B., Eriksson K., Mizuno-Wiedner M., Jørgensen U. G., Plez B., 2003, in Hubeny I., Mihalas D., Werner K., eds, ASP Conf. Ser. Vol. 288, Stellar Atmosphere Modeling. Astron. Soc. Pac., San Francisco, p. 331
Hebb L., Wyse R. F. G., Gilmore G., Holtzman J., 2006, AJ, 131, 555
Herbst W., Bailer-Jones C. A. L., Mundt R., Meisenheimer K., Wackermann R., 2002, A&A, 396, 513
Hillenbrand L., 1997, AJ, 113, 1733
Hinkle K. H., Cuberly R. W., Gauhan N. A., Heynssens J. B., Joyce R. R., Ridgway S. T., Schmitt P., Simmons J. E., 1988, in Fowler A. M., ed., Proc. SPIE, Vol. 3354, Infrared Astronomical Instrumentation. SPIE, Bellingham WA, p. 810

Hodgkin S. T., Irwin J. M., Aigrain S., Hebb L., Moraux E., Irwin M. J., 2006, Astron. Nachr., 327, 9

Honeycutt R. K., 1992, PASP, 104, 435

Irwin J., Aigrain S., Hodgkin S., Irwin M., Bouvier J., Clarke C., Hebb L., Moraux E., 2006, MNRAS, 370, 954

Irwin J., Irwin M., Aigrain S., Hodgkin S., Hebb L., Moraux E., 2007, MNRAS, 375, 1449

Jones B. F., Walker M. F., 1988, AJ, 95, 1755

Lane B. F., Boden A. F., Kulkarni S. R., 2001, ApJ, 551, 81

Leggett S. K., 1992, ApJS, 82, 351

Lopez-Morales M., 2004, PhD thesis, Univ. North Carolina

Lopez-Morales M., Orosz J. A., Shaw J. S., Havelka L., Arevalo M. J., McIntyre T., Lazaro C., 2006, ApJ, preprint (astro-ph/0610225)

Lucy L. B., 1967, Z. Astrophys., 65, 89

Mazeh T., Prato L., Simon M., Goldberg E., Norman D., Zucker S., 2002, ApJ, 564, 1007

Mullan D. J., MacDonald J., 2001, ApJ, 559, 353

Nelson B., Davis W. D., 1972, ApJ, 174, 617

Palla F., Stahler S. W., 1999, ApJ, 525, 772

Palla F., Randich S., Pavlenko V., Flaccomio E., Pallavicini R., 2007, ApJ, 659, 41

Pont F., Bouchy F., Melo C., Santos N. C., Mayor M., Queloz D., Udry S., 2005, A&A, 438, 1123

Popper D. M., Etzel P. B., 1981, AJ, 86, 102

Press W. H., Teukolsky S. A., Vetterling W. T., Flannery B. P., 1992, Numerical Recipes in FORTRAN 77: The Art of Scientific Computing. Cambridge Univ. Press, Cambridge, p. 402

Rebull L. M., Stauffer J. R., Megeath S. T., Hora J. L., Hartmann L., 2006, ApJ, 646, 297

Ségransan D., Kervella P., Forveille T., Queloz D., 2003, A&A, 397, 5

Sicilia-Aguilar A. et al., 2005, AJ, 129, 363

Siess L., Forestini M., Dougados C., 1997, A&A, 324, 556

Siess L., Dufour E., Forestini M., 2000, A&A, 358, 593

Simon K. P., Sturm E., 1994, A&A, 281, 286

Southworth J., Maxted P. F. L., Smalley B., 2004a, MNRAS, 351, 1277

Southworth J., Zucker S., Maxted P. F. L., Smalley B., 2004b, MNRAS, 355, 986

Southworth J., Smalley B., Maxted P. F. L., Claret A., Etzel P. B., 2005, MNRAS, 363, 529

Stassun K. G., Mathieu R. D., Mazeh T., Vrba F. J., 1999, AJ, 117, 2941

Stassun K. G., van den Berg M., Mathieu R. D., Verbunt F., 2002, A&A, 382, 899S

Stassun K. G., Mathieu R. D., Vaz L. P. R., Stroud N., Vrba F. J., 2004, ApJS, 151, 357

Stassun K. G., Mathieu R. D., Valenti J. A., 2006, Nat, 440, 311

Stassun K. G., Mathieu R. D., Valenti J. A., 2007, ApJ, preprint (astro-ph/0704.3106)

Tody D., 1993, in Hanisch R. J., Brissenden R. J. V., Barnes J., eds, ASP Conf. Ser. Vol. 52, Astronomical Data Analysis Software and Systems II. Astron. Soc. Pac., San Francisco, p. 173

Tonry J., Davis M., 1979, AJ, 84, 1511

Yi S., Demarque P., Kim Y.-C., Lee Y.-W., Ree C. H., Lejeune T., Barnes S., 2001, ApJS, 136, 417

This paper has been typeset from a TeX/LaTeX file prepared by the author.